IEEE Robotics and Automation Letters (RA-L) paper, presented at ICRA 2024, Yokohama, Japan. Cite as RA-L paper.

Magnetic Gear-based Actuator: A Framework of Design, Optimization, and Disturbance Observer-based Torque Control

Hangyeol Song[1], Edgar Lee[1], Hyung-Tae Seo[2]*, and Seokhwan Jeong[1]*, *Member, IEEE,*

***Abstract*—This letter presents a design framework and novel control strategy for a compact coaxial magnetic-gear-based actuation module suitable for small-to-mid-sized mechanical and robotic applications. The proposed actuation module adopts a non-contact magnetic coupling mechanism to transmit rotational power with a predetermined gear ratio, in contrast to traditional mechanical gear-based transmissions. This approach offers several advantages such as enhanced backdrivability, hardware safety, and transparency when compared to conventional contact-based transmissions. Furthermore, the magnetic coupling effect provides a spring-like characteristic that can be utilized to implement a series elastic actuation enabling sensorless torque control. The design of the magnetic gear was optimized using a differential evolution method, and a dynamic model was formulated to specify its dynamic characteristics. Finally, a composite disturbance observer-based torque control algorithm was developed, which capitalizes on the features of the magnetic spring. The proposed control algorithm was validated through several experiments.**

***Index Terms*—Actuation and Joint Mechanisms, Mechanism Design, Compliant Joints and Mechanisms, Force Control**

I. Introduction

In robotic applications, an input-output transmission ratio shifting mechanism, normally called a transmission (e.g., planetary gear train and harmonic drive, etc.), is widely used to align the actuator's nominal operating range and the system's required operating range. The conventional transmission mechanisms have been implemented by mechanical gearing to transmit the power; however, the contact manner may cause noise, friction, and backlash, which decreases the lifespan, transparency, and backdrivability as the transmission ratio increases. Additionally, these mechanisms require lubrication and frequent maintenance.

As an alternative to the contact-based transmission, a magnetically driven transmission has gotten attention, providing a non-contact power transmission feature. The concept of magnetically driven transmission, so-called magnetic gear, was proposed in 1980-1990 [1], [2]. Its inherent non-contact power transmission manner provides a backdrivability of the actuation system, which is robust to external impact and acts like a torque limiter; and it is free from the issues caused by noise, friction, heat, and maintenance such as lubrication, which are considered drawbacks of the conventional contact-based transmission.

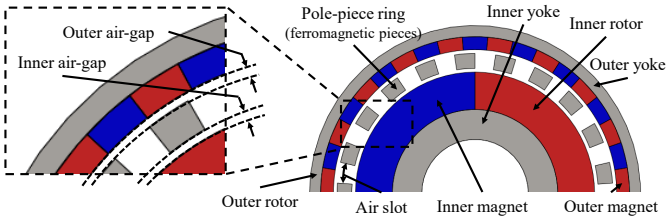

Fig. 1: Geometry of coaxial magnetic gear

Since Atallah has proposed a high-performance *coaxial magnetic gear* design with enhanced torque density using a modulation ring [3], [4], the magnetic gear-based transmission has gotten more attention from other researchers; and its mathematical modeling [5], parametric optimization [6], [7], and effect of cogging torque [8] have been investigated by research groups. [9] compared magnetic gears with mechanical planetary gears, and [10] showed an effect of magnet grade, temperature, and gear ratio in coaxial magnetic gear. The non-contact transmission feature of magnetic gears has found applications in various fields, including wind power generators [11], electric air propulsion [12], and yacht propellers [13]. Further, [14] suggested a linear electromagnetic actuator using the concept of magnetic screw transmission, [15] showed consequent pole cycloidal magnetic gear for aerospace applications, and [16] proposed a mechanically variable magnetic gear transmission system for robotic applications. While most of the magnetic gear-based applications have been implemented for medium to large-scale systems, few trial has been reported for small to mid-sized mechanical and robotic systems due to its relative low torque density and high complexity.

Some researchers addressed control strategies for the magnetic gear systems. Atallah et al. targeted servo control problems with a dual observer-based approach [17], [18] and focused on pole-slip recovery and prevention to avoid negative stiffness using a slip detection algorithm and a model predictive controller (MPC) [19]. However, their control strategy was focused on position control rather than force control, and their

Manuscript received: April, 13, 2023; Revised July, 12, 2023; Accepted August, 12, 2023. This paper was recommended for publication by Editor J. P. Desai upon evaluation of the Associate Editor and Reviewers' comments. This work was supported by the National Research Foundation of Korea (NRF) grant funded by the Korea Government (MSIT) (No.2021R1F1A1046838 and RS-2023-00218379) and the Technology Innovation Program (20018274) funded By the Ministry of Trade, Industry & Energy (MOTIE, Korea) *(Hangyeol Song and Edgar Lee contributed equally to this work.) (Corresponding author: H. -T. Seo and S. Jeong)*

[1]H. Song, E. Lee, and S. Jeong are with Department of Mechanical Engineering, Sogang University, Seoul, South Korea (e-mail: lnhgf9@sogang.ac.kr; edgarlee21@sogang.ac.kr; seokhwan@sogang.ac.kr).

[2]H. -T. Seo is with the Department of Mechanical Engineering, Kyonggi University, Suwon-si, South Korea (e-mail: htseo@kyonggi.ac.kr).

Digital Object Identifier (DOI): see top of this page.

IEEE Robotics and Automation Letters (RA-L) paper, presented at ICRA 2024, Yokohama, Japan. Cite as RA-L paper.

TABLE I: Comparison of Controller

-	[17]	[18]	[19]	[20], [21]	proposed
Control Target	Spd	Pos	Spd	Spd/Tor	Tor
F/T Estimation	-	State estimation using observer			Deflection angle
Pole-slip	D,R	N/A	D,R,P	N/A	D,R

Spd = speed; Pos = position; Tor = torque; D = detection; R=recovery; P = prevention; N/A = information not available;

analysis only considered a magnetic gear system with a gear ratio of 1:1 to simplify the dynamics. Their pole-slip recovery method showed excellent results under constant speed control; still, the MPC required much computational power. Komiyama et al. studied the robotic application of magnetic spur gear from estimating contact force using magnetic coupling to hybrid control [20], [21]. To estimate the external contact force, a force observer was designed with the model from a motor input to a motor angle, assuming the magnetic gear as an ideal low gear ratio system while ignoring friction. However, the state estimate-based force control strategy could be severely affected by the modeling error of the system.

In summary, although the several design and control of magnetic gears have been studied in the past decades, very few research has been reported for a general design and control framework for small to medium-sized general mechanical or robotic applications, considering proper transmission ratio, optimal design, and force control for the nonlinear dynamics, simultaneously. In particular, the inherent nonlinearity of magnetic gear makes it challenging to control torque precisely, which has not been sufficiently addressed.

This letter introduces a framework for the coaxial magnetic gear actuation module suitable for small to medium-sized mechanical or robotic applications, based on our preliminary prototyping [22]. The paper presents 1) a mechanical design and an optimization procedure of the actuation module, 2) the characteristics of magnetic coupling of coaxial magnetic gear, and 3) a disturbance observer(DOB)-based torque control framework that enables its practical use in mechanical and robotic applications. The proposed force control methodology utilizes a spring-like characteristic (i.e., called *magnetic spring*), which originates from the magnetic coupling of the magnetic gear. This feature, similar to a series elastic actuator (SEA), enables the sensing and controlling of contact force without the need for external torque sensors. By directly controlling the deflection angle of the magnetic spring, the proposed approach enables more precise and straightforward force control with high bandwidth compared to the previous control methodology [17]–[21], while the DOB loop we proposed help to linearize the nonlinearity of the magnetic gear. Furthermore, controlling the deflection angle of the magnetic spring simplifies the detection and recovery of pole-slip. Table. I represents the brief comparison of controller. The details are presented in this letter.

This letter is organized as follows with supplementary videos (Videos S1-S3), Section II describes the optimization procedure guideline and mechanical design of the actuation module briefly. The dynamic model is presented in Section III, followed by the torque control algorithm using magnetic coupling in Section IV. Section V represents the validation of the proposed controller through various experiments. The discussion and conclusion are followed in Section VI and VII.

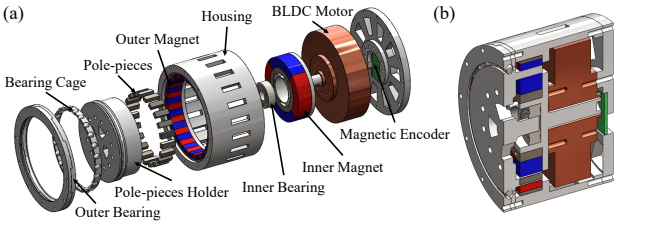

Fig. 2: Schematic diagram of the proposed magnetic gear based actuator: (a) exploded view, (b) cross-section view

II. Design and Optimization

For small-to-mid-sized mechanical and robotic applications, the prototype of the magnetic-gear-based actuation module was designed with a compact disc-type direct drive BLDC motor based on our preliminary work [22].

The magnetic gear was employed as a transmission connecting the motor and the output, amplifying the torque. This section presents the working principle of the coaxial magnetic gear, optimization procedure guideline, and mechanical design of the proposed magnetic gear-based actuation module.

A. Working Principle of Coaxial Magnetic Gear

Let us review the working principle of the coaxial magnetic gear. The conventional coaxial magnetic gear, as depicted in Fig. 1, consists of three parts: the inner rotor, the outer rotor, and the pole-piece ring. The inner and outer rotors have a particular arrangement of magnets that create harmonic orders corresponding to each magnetic pole pair in the inner and outer air-gaps, respectively. The pole-piece ring, also known as the modulation ring, is made up of a specific number of ferromagnetic pieces. This unique configuration modulates the harmonic order produced by each rotor and forms the same number of harmonic orders of the counterpart rotor in each counterpart air-gap, resulting in magnetic coupling between the rotors [3]. By utilizing this magnetic gear configuration, we have introduced a magnetic gear-based actuation module, as illustrated in Fig. 2 (further details will be discussed in Sec. II-C). The magnetic coupling is established with a specific transmission ratio, G, between the input and output, which depends on which part is set to be stationary (i.e., fixed to ground). The formulas for calculating G are as follows [16]:

$$N = p_i + p_o \tag{1}$$

$$G = \begin{cases} w_o/w_N = N/p_o & \textbf{Case1: inner rotor fixed} \\ w_i/w_N = N/p_i & \textbf{Case2: outer rotor fixed} \\ w_i/w_o = -p_o/p_i & \textbf{Case3: pole-piece ring fixed} \end{cases} \tag{2}$$

where p_i and p_o are the number of pole pairs of the inner and outer rotor, and N is the number of pole-pieces. w_i, w_o, and w_N are the rotational velocity of the inner rotor, outer rotor, and pole-piece ring, respectively. The negative sign of the transmission ratio represents a reverse rotation. Note that this feature is remarkably similar to the planetary gear train.

To comprehend more intuitively, the magnetic gear could be considered having virtual gear teeth whose number corresponds to the number of the pole pairs. For example, Fig. 3(a)-(b) shows a comparison between the conventional spur

IEEE Robotics and Automation Letters (RA-L) paper, presented at ICRA 2024, Yokohama, Japan. Cite as RA-L paper.

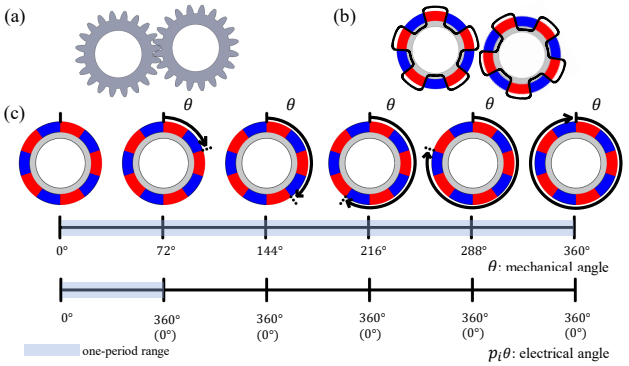

Fig. 3: Comparison between (a) conventional spur gear and (b) magnetic gear and (c) relation between the mechanical and electrical angles.

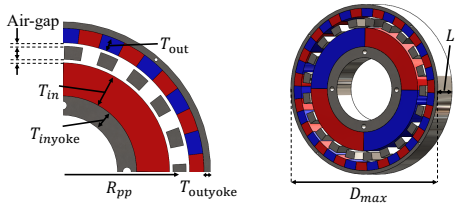

Fig. 4: Design parameters of the magnetic gear in optimization procedure.

gear and magnetic gear without a modulation ring (i.e., the gear ratio is 1:1). The solid line of Fig. 3(b) represents the flux density distribution along the circular direction, which could be regarded as the virtual gear teeth; and each virtual gear teeth is repeated for each period of electrical angle. Fig. 3(c) shows the relation between the mechanical angle, θ, and the electrical angle. While θ varies a one-period ranging from 0° to 360°, the corresponding electric angle varies from from 0° to $p_i\theta$, having multiple number (i.e., p_i) of a one-period due to repeated polarities of the magnetic gear. As illustrated in Fig. 3(c), during the one-period of θ, the electric angle has five cycles, where the polarity of the magnet is repeated at $\theta = [0^\circ, 72^\circ, 144^\circ, 216^\circ, 288^\circ, 360^\circ]$.

B. Optimization

In this study, the gear ratio is set to be G = 10.5, similar to that of planetary gear-based actuation modules for small-to-mid-sized mobile robots [23]. The number of pole pairs and pole pieces were chosen as p_i=2, p_o=19, and N=21 considering the ripple factor [24]. It represents the magnitude of the ripple and is expressed as a function of the number of pole pairs and the number of pole pieces (i.e., p_i and N). The formulation is as follows:

$$R_{F,2} = \frac{2P_i}{LCM(2p_i, N)} \tag{3}$$

where LCM represents a least common multiple, and $R_{F,2}$ is a ripple factor of the pole-piece ring. As the ripple factor increases, the magnitude of the ripple tends to increase. In this letter, $R_{F,2}$ was designed to have minimized value (i.e., $2p_i$ and N are relatively coprime number) to avoid a large ripple.

Although (2) provides a primary relationship between input and output, the maximum transmittable torque needs to be specified with various design parameters. To simplify the optimization procedure and maximize the transmittable torque within a limited actuation volume, we chose dominant

TABLE II: Design Parameters of the Magnetic Gear in Optimization

Symbol	Design variables	Range	Opt. Value	Unit
T_{in}	Thickness of inner magnet	1∼10	10	mm
T_{out}	Thickness of outer magnet	1∼10	4.4	mm
T_{pp}	Thickness of pole pieces	1∼10	4	mm
T_{inyoke}	Thickness of inner yoke	1∼10	5.8	mm
$T_{outyoke}$	Thickness of outer yoke	1∼10	2	mm
R_{pp}	Position of pole pieces	20∼40	35.6	mm
D_{max}	Maximum diameter	-	90	mm
L	Axial length	-	15	mm
–	Inner/outer air-gap	-	1	mm
p_i	Pole-pairs of inner rotor	-	2	-
p_o	Pole-pairs of outer rotor	-	19	-
N	Number of pole pieces	-	21	-

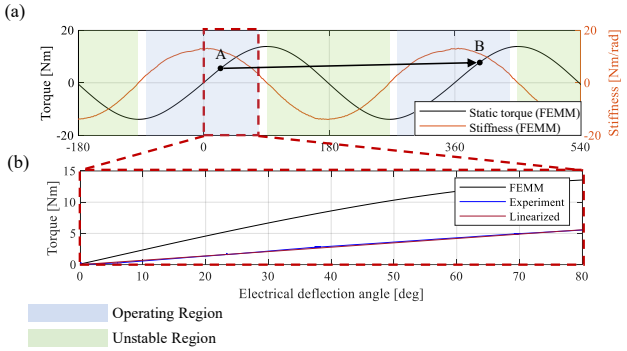

Fig. 5: Static torque of optimized magnetic gear and its stiffness (a) using 2D FEM, (b) comparison between 2D FEM and experiment result

optimization parameters from the previous studies, which affect the output torque significantly [6], [7]. The six design parameters were chosen (see Fig. 4) and summarized in Table II.

The object function was set to maximum static torque, directly relevant to maximum transmittable torque of output (i.e., pole-piece ring). The static torque was calculated in each iteration using the 2D finite element method magnetics (FEMM) [25] to make optimization more straightforward and time-saving rather than solving infinite summation expressions as objective functions [5]. The optimized result shows that the maximum transmittable torque increase approximately up to ≈14 Nm. Further information is available in our previous prototyping [22].

C. Mechanical Design

The overall schematic diagram of the proposed actuation module is shown in Fig. 2. To maximize the gear ratio, the outer rotor was fixed, and the inner rotor and the pole-piece holder (ring) were set as the input and output, respectively, as determined by (2). Both the inner and outer rotors have built-in neodymium magnets (NdFeB, Grade: N40), while the pole-piece ring and the inner and outer yokes were made of laminated silicon steel (50PN1300, 0.5mm thickness). The inner ball bearing was made of 304 stainless steel to reduce flux leakage, while the remaining parts were 3D printed using ABS plastic (style NEO-A22C, CUBICON). A disk-type direct drive BLDC motor (ϕ 92.3mm×38mm, 200W, 0.8Nm) served as the input source for the module, and the angular position of the motor was measured by a 12-bit magnetic encoder (AS5600, AMS). The overall parameters of the actuator are summarized in Table. III.

IEEE Robotics and Automation Letters (RA-L) paper, presented at ICRA 2024, Yokohama, Japan. Cite as RA-L paper.

TABLE III: Parameters of the Magnetic Gear-Based Actuation Module

Symbol	Parameter	Value	Unit
D_{module}	Diameter of actuation module	106	mm
L_{module}	Height of actuation module	76	mm
-	Weight of actuation module	1.3	kg
-	Weight of motor	0.53	kg
-	Nominal power of motor	200	W
-	Nominal torque of motor	0.8	Nm
J_m	Inertia of motor side	$5.508e-3$	$kg \cdot m^2$
J_l	Inertia of load side	$0.142e-3$	$kg \cdot m^2$
B_m	Damping of motor side	$2.24e-6$	$Nm \cdot s/rad$
B_l	Damping of load side	0.0885	$Nm \cdot s/rad$
K_f	Linearized magnetic spring stiffness	4	Nm/rad

III. DYNAMICS ANALYSIS AND MODELING

This section describes the dynamic analysis of the magnetic gear, mainly focusing on spring-like characteristics (i.e., such as SEA) and modeling as a two mass-spring system.

A. Spring Characteristics of Magnetic Gear

The magnetic coupling of the magnetic gear provides spring-like characteristics (i.e., magnetic spring), which is illustrated well in the static torque plot. Fig. 5(a) shows the static torque, τ, of the optimized magnetic gear depending on the electrical deflection angle between the input and the output, θ_e, using FEMM. The static torque and the electric deflection angle were calculated as follows [17]:

$$\tau = \tau_g \sin(\theta_e) \tag{4}$$

$$\theta_e = p_i \theta_m - N\theta_l \tag{5}$$

where θ_m and θ_l are the rotational angles of a motor and load side (i.e., inner rotor: input, pole-pieces ring: output), τ_g is the peak torque of the sine wave.

Equation (4) implies that there is an elastic component like a virtual spring between the input and output, and we call it *magnetic spring*. The magnetic spring is assumed to be the non-linear spring, which creates sinusoidal stiffness relative to the θ_e as shown orange line in Fig. 5(a). This feature is an essential factor for overload protection. When an excessive torque is applied to the actuation module and θ_e exceeds the angle at the peak of the sine wave, the magnetic coupling falls apart between the input and output, which induces pole-slip without damaging parts.

Here, we assumed that the non-linear spring is considered a linear spring with stiffness K_f, and (4) can be approximated as follow within a confined range of θ_e:

$$\tau_{spring} = K_f \theta_e \tag{6}$$

Due to the unstable region where stiffness has a negative value (see the green region in Fig. 5(a)), we restricted the θ_e in a range between $-80°$ and $80°$ with $10°$ margin from the unstable regions (i.e., $\pm 90°$) to guarantee the stability of the system, as depicted as the blue region in Fig. 5(a). The linearized stiffness was obtained from the experiment, and the result is illustrated in Fig. 5(b) and Table. III.

In Fig. 5(b), we could observe relatively large differences between the 2D FEMM result and the experiment result, whose maximum transmittable torque is 43% of 2D FEMM. The discussion section will address the reasons for this discrepancy.

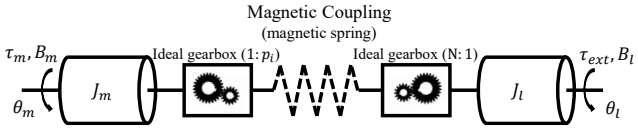

Fig. 6: Simplified model of actuation module

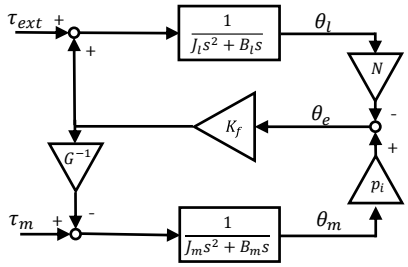

Fig. 7: Block diagram of the actuation module as a two-mass system

B. Two Mass-Spring System Modeling

Based on the magnetic spring feature discussed in section III-A, the actuation module was modeled as a two mass-spring with an ideal gearbox, as shown in Fig. 6. Its dynamic equations can be derived as follows [17]:

$$J_m \frac{d\omega_m}{dt} = -B_m \omega_m - \frac{K_f}{G}(p_i \theta_m - N\theta_l) + \tau_m \tag{7}$$

$$J_l \frac{d\omega_l}{dt} = -B_l \omega_l - K_f(N\theta_l - p_i \theta_m) + \tau_{ext} \tag{8}$$

where J_m, B_m, J_l, and B_l are the rotational inertia and damping coefficient of motor and load side, respectively. Note that J_m is the lumped the inertia of the motor and inner rotor. τ_m and τ_{ext} represent the motor and external torque.

Fig. 7 illustrates a block diagram of the actuation module as a two-mass system. It consists of motor side dynamics, load side dynamics, and the magnetic spring that couples the motor and load side dynamics, similar to a SEA. The relationship between input (i.e., τ_m) and various outputs (i.e., θ_m, θ_l, and θ_e) could be derived from the block diagram Fig. 7.

$$\frac{\theta_m}{\tau_m} = \frac{J_l s^2 + B_l s + K_f N}{D(s)} \tag{9}$$

$$\frac{\theta_l}{\tau_m} = \frac{K_f p_i}{D(s)} \tag{10}$$

$$\frac{\theta_e}{\tau_m} = \frac{p_i J_l s^2 + p_i B_l s}{D(s)} \tag{11}$$

where $D(s)$ is the characteristic equation of the system, represented as follows:

$$\begin{aligned} D(s) = & J_m J_l s^4 + (J_m B_l + J_l B_m) s^3 \\ & + (J_m K_f N + B_l B_m + J_l K_f p_i / G) s^2 \\ & + (K_f N B_m + K_f p_i B_l / G) s \end{aligned} \tag{12}$$

The actual parameters were identified by using System Identification Toolbox (MATLAB R2022a, Mathworks) by applying a chirp signal input and measuring the output. The parameters are listed in Table III. Note that the system includes a single arm with a mass attached to the end. The arm length and the mass weight are 32cm and 500g, which replicates an application in a robotic (or mechanical) system.

IEEE Robotics and Automation Letters (RA-L) paper, presented at ICRA 2024, Yokohama, Japan. Cite as RA-L paper.

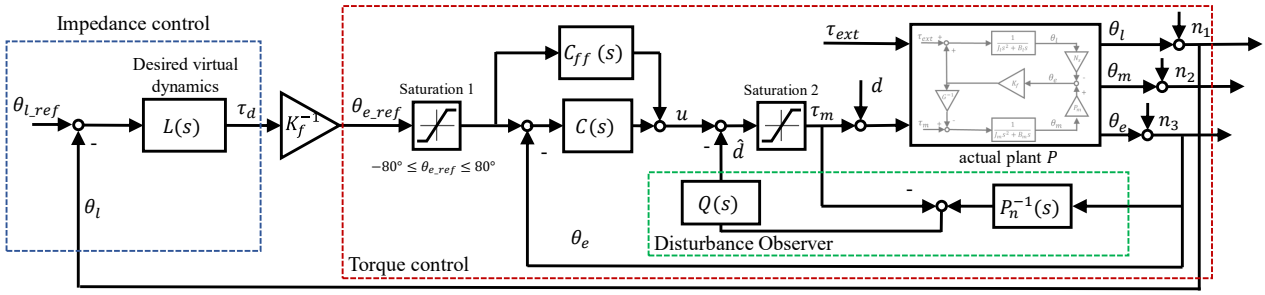

Fig. 8: Block diagram of the proposed control algorithm

IV. Torque Control Based on Dynamic Model

In this section, we propose a novel torque control strategy of the proposed magnetic gear actuation module exploiting the magnetic spring feature based on the dynamic model derived in section III-B.

A. Torque Control: disturbance observer

As shown in section III-B, the relationship between the torque and electrical deflection angle in (4) implies that it is possible to control the torque by controlling the position instead of direct torque control using extra torque/force sensors; therefore, the magnetic-geared actuator can be treated as a SEA, and we can apply the force control strategies employed for SEAs. In addition, for high-performance torque control, we propose composite DOB-based control and feedforward controller algorithm exploiting the magnetic spring as shown in Fig. 8.

In order to design the controller, a nominal plant was derived. We assumed the inertia of the load side is infinite (i.e., $J_l = \infty$ and $\theta_l = \dot{\theta}_l = 0$) to simplify the torque controller design and replicate the situation when the load side comes into contact with the ground, whereby the nominal plant (i.e., P_n) is derived from (11) as follows:

$$P_n = \frac{\theta_e}{\tau_m} = \frac{p_i}{J_m s^2 + B_m s + K_f p_i / G} \tag{13}$$

However, the magnetic gear is composed of multiple nonlinearities such as nonlinear characteristics of the magnetic spring and the customized 3D printed bearing friction, which results in a discrepancy between the nominal model and the actual plant. Additionally, signal noises are imposed at sensor measurement. These nonlinear factors and measurement noises are represented as disturbance, d, noise, $n_{1,2,3}$ respectively, in Fig. 8. To nominalize the actual plant and attenuate disturbances and noise, a DOB loop using a Q-filter approach has been implemented, providing a disturbance estimate, $\hat{d}$ [26]–[28]. By implementing the active disturbance rejection, the output of the loop is derived from the block diagram Fig. 8.

$$\theta_e = \frac{PP_n}{P_n(1-Q)+PQ}u + \frac{PP_n(1-Q)}{P_n(1-Q)+PQ}d + \frac{-PQ}{P_n(1-Q)+PQ}n_3 \tag{14}$$

where P is the actual plant and P_n is the nominal plant of system. The u is controller output, which is equivalent to $C_{ff}\theta_{e\_ref} + C(\theta_{e\_ref} - \theta_e)$ in Fig. 8 (here, the role of C_{ff} will be discussed later).

Depending on the Q-filter, (14) is formulated as follows.

$$\theta_e = P_n u - n_3 \qquad \text{where } Q(s) \approx 1 \tag{15}$$

$$\theta_e = Pu + Pd \qquad \text{where } Q(s) \approx 0 \tag{16}$$

Equation (15)-(16) means that DOB removes the inherent nonlinearity in the magnetic gear (when $Q \approx 1$) and attenuates signal noise (when $Q \approx 0$) so that the system behaves like a nominal linear plant obtained in (13). The performance of the DOB is mainly determined by the Q-filter which is usually a stable low-pass filter with the unity dc gain. Many factors are considered in designing the Q-filter, such as system bandwidth, stability, and nominal plant, etc. In this letter, 3rd order low-pass Butterworth filter was employed as a Q-filter with a cut-off frequency of 30 Hz, based on the system bandwidth, relative degree of the nominal plant, and effective noise attenuation.

B. Torque Control: PD and feedforward controller

Once the system was nominalized by DOB, a feedback controller was implemented. The proportional-derivative (PD) controller, C, was adopted for feedback, and the controller gains were given by the nominal plant. Regardless, an additional controller is required since the system is of type 0 (meaning there is a steady-state error when a step input is applied). Rather than adding an integral gain, we introduced feedforward terms, C_{ff}, to remove the steady-state error and increase the bandwidth of closed loop. This approach enhances the ability of the actuator to track the step reference more quickly and stably than utilizing an integral gain [27], [28]. If we only consider steady-state situation (i.e., $s \to 0$), the feedforward controller may be designed as follows:

$$\lim_{s\to 0} C_{ff}(s)P_n(s) = 1 \tag{17}$$

$$C_{ff} = K_f / G \tag{18}$$

The C_{ff} could be derived as $P_n^{-1}Q$ to compensate for a wide range of frequency references (i.e., $s \neq 0$). However, this could increase the complexity of C_{ff}, resulting in a large control input from C_{ff}, which can surpass the saturated control input from the 2nd saturation block in Fig. 8 due to the limit of the system and makes an undesirable response. Thus, we chose the constant $C_{ff} = K_f/G$ to make the controller simpler and avoid the unintended response. The steady-state error resulting from a unit step input, e_{ss}, is calculated as follows.

$$e_{ss} = \lim_{s\to 0} \frac{1 - C_{ff}(s)P_n(s)}{1 + C(s)P_n(s)} = 0 \tag{19}$$

IEEE Robotics and Automation Letters (RA-L) paper, presented at ICRA 2024, Yokohama, Japan. Cite as RA-L paper.

IEEE Robotics and Automation Letters (RA-L) paper, presented at ICRA 2024, Yokohama, Japan. Cite as RA-L paper.

C. Pole-slip Detection and Recovery

Pole-slip is the feature that makes controlling the magnetic gear difficult but also ensures hardware safety. This occurs when the sum of control input and external impact exceeds the maximum transmittable torque of the system. To tackle this issue, we adopted two solutions. 1) The reference of the electrical deflection angle (i.e., θ_{e_ref}) should be within a range of $-80^\circ \sim 80^\circ$, as discussed in section III-A. This is implemented and depicted as the 1st saturation block in Fig. 8. 2) The electrical deflection angle (i.e., θ_e) was modified to be within a range of -180° $\sim$ 180° to control the torque after the pole-slip. When pole-slip occurs, (6) is no longer applicable, and it is necessary to shift and correct the operating region. As the electrical deflection angle is measured directly, pole-slip can be easily detected. The modified electrical deflection angle can therefore be calculated as follows.

$$\theta_{e.mod} = \begin{cases} \theta_e & \textbf{(no pole-slip)} \\ \theta_e - 2n\pi & \textbf{(n times positive pole-slip)} \\ \theta_e + 2n\pi & \textbf{(n times negative pole-slip)} \end{cases} \quad (20)$$

For instance, in Fig. 5(a), the occurrence of pole-slip will result in the movement of point A to point B, which is one time positive pole-slip. In this case, $\theta_{e.mod}$ is calculated and corrected as $(\theta_e - 2\pi)$. Note that $\theta_{e.mod}$ was only used for actual controller implementation because it is a particular case. In this letter, θ_e was used for generality.

D. Impedance Control Algorithm

In order to validate the feasibility of the performance of the actuation system under interaction with the environment, an impedance controller was introduced based on the torque control algorithm to make the desired virtual dynamics between the environment and the load side. Since the electrical deflection angle, θ_e, provides torque information, the impedance controller can be easily implemented regarding the load side angle, θ_l. The most outer loop of the controller (see Fig. 8) illustrates the block diagram of the impedance controller. θ_l is feedback and subtracted from the desired trajectory (i.e., θ_{l_ref}), and the desired impedance, $L(s)$, is multiplied.

$$L(s) = K_d + C_d s \quad (21)$$

where K_d and C_d are the desired stiffness and the damping coefficient. It produces torque references that is imposed to the torque controller discussed in section IV-A. The following section describes experimental and validation result.

V. Experiments

The proposed actuation module and the controller were validated through several experiments. Fig. 9 shows the experiment setup where Fig. 9(a) describes the torque tracking experiment setup and Fig. 9(b) describes the impedance and overload protection setup. The experimental setup includes a motor driver (ESCON module 50/8, Maxon) to operate the disk-type direct drive BLDC motor used as the input source in current control mode and a microcontroller (LAUNCHXL-F28379D, Texas Instruments) for embedding control algorithm. The extra encoder (AMT103-V, CUI) was embedded to measure θ_l, and the loadcell (BDCM-100, BONGSHIN) was used to measure output torque. The experimental data were obtained using Simulink (MATLAB R2022a, Mathworks) via a data acquisition system (National Instrument, PCIe-6321). Three experiments were conducted, and the results are described in the following section.

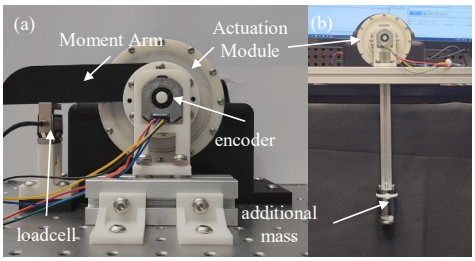

Fig. 9: Experiment setup (a) in torque tracking performance under quasi-static condition, (b) in impedance and overload protection under dynamic condition

A. Torque Control with DOB

In Experiment 1, a square waveform torque reference was applied to two different controller configurations: 1) PID controller only and 2) PD+DOB controller with feedforward controller. Fig. 10(a)-(b) shows the tracking performance and error of both controllers. Although both show zero steady-state error, the proposed controller shows a much faster and desirable transient response, similar to the simulation result. Compared to the designed controller, the PID controller compensates for steady-state error using the integral term, which decreases margins. In Fig. 10(c), the measured torque and the estimated torque from θ_e are represented, and it shows a very accurate force reference tracking result.

To figure out the torque bandwidth of the both controllers, the frequency response of the system was measured (see Fig. 11). The sinusoidal torque reference with various frequencies (i.e., 0.01 to 30Hz) was applied, and the electrical deflection angle, θ_e, was measured simultaneously. The bandwidths of both controllers were approximately 1Hz (PID) and 8Hz (PD+DOB with FF), which showed a significant improvement.

Note that this experiment assumed quasi-static dynamics (i.e., the movement of the load side is small due to the loadcell), and the desired torque reference was always above zero because of the measurement setup.

B. Impedance Control

In Experiment 2, we measured the load side angle with the given reference to figure out the effect of the impedance controller. Fig. 12 represents the load side angle depending on the various impedance conditions (i.e., K_d and C_d). On the load side, additional 0.5kg mass was attached to the 32cm moment arm, as shown in Fig. 9(b). When a square waveform reference (i.e., equilibrium position) was applied to the load side angle, various system responses were observed depending on the different impedance conditions, as illustrated in Fig. 12. During the experiment, the gravity of the moment arm and additional mass were imposed on the system as a disturbance. As the impedance gain increases, the system response was closer to the reference. Understandably, high impedance gain

IEEE Robotics and Automation Letters (RA-L) paper, presented at ICRA 2024, Yokohama, Japan. Cite as RA-L paper.

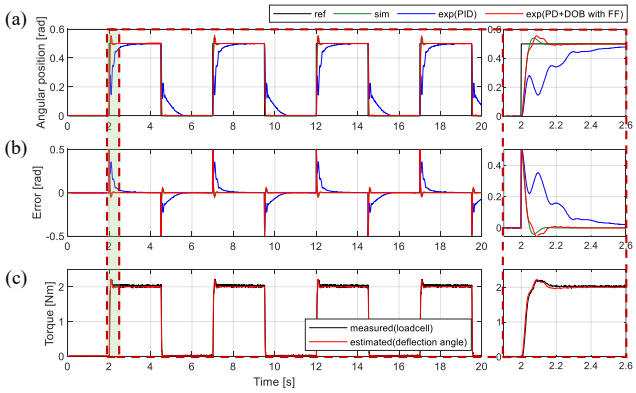

Fig. 10: Result of torque control experiments: comparison of (a) reference tracking measured response of electrical deflection angle between PID controller and PD+DOB with FF controller and (b) error of both controllers. (c) Measured and estimated output torque using PD+DOB with FF controller

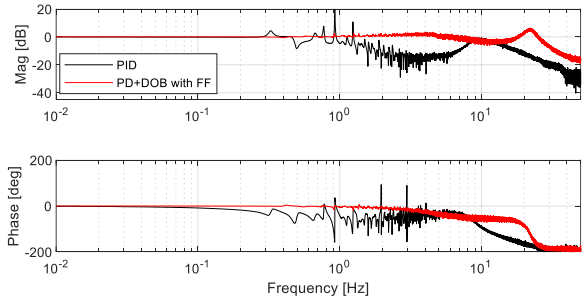

Fig. 11: Frequency response of torque control loop: (a) PID controller (b) PD+DOB with FF controller

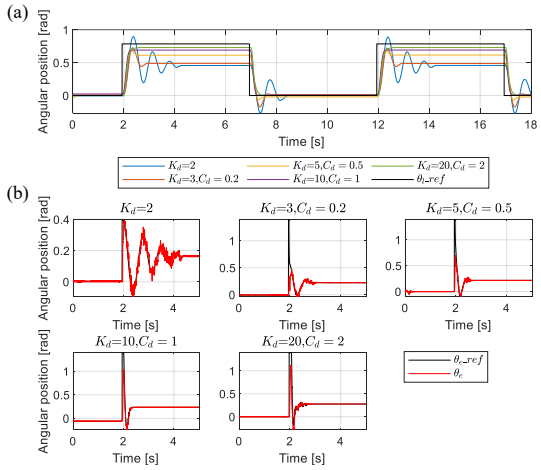

Fig. 12: System response depending on various desired impedance: (a) load side angle and (b) electrical deflection angle

leads to robust disturbance rejection. The results of this experiment demonstrated the ability to achieve various impedance conditions, thereby indicating the versatility of the proposed system in adapting to different applications. The demonstration video shows various impedance control achieved (see the Video S1 and S2).

C. Overload Protection and Pole-slip Recovery

In Experiment 3, we validated the overload protection property that is the prominent feature of the magnetic gear and the behavior of the actuator after pole-slip occurred (i.e., pole-slip recovery). A large impact was exerted while the actuation

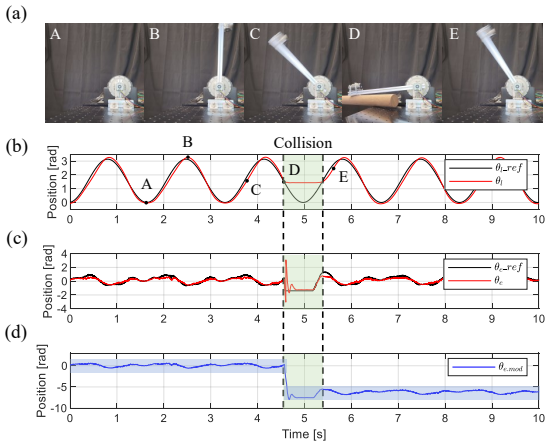

Fig. 13: System behavior when the overload applied: (a) experiment setup, (b) reference tracking response of the desired load-side angle, (c) electrical deflection angle and (d) unmodified electrical deflection angle

module followed the desired reference with an impedance control gain (i.e., K_d=10, C_d = 1), as shown in Fig. 13. When the overload was enforced (i.e., unexpected collision with an object), the magnetic coupling instantaneously broke apart (i.e., pole-slip), keeping the hardware safe (see point D in Fig. 13). In Fig. 13(c), the pole-slip caused the spike since we modified its angle from $-180°$ to $180°$ range. As shown in Fig. 13(d), the unmodified electrical deflection angle represents the operation region shifting obviously (see the blue region in Fig. 13(d)). After occurring the pole slip, the controller automatically re-engaged magnetic coupling since our proposed controller directly controls the electrical deflection angle of the actuator. Thanks to the pole slip, there was no noticeable damage to the system (see the Video S3)

VI. Discussion

We presented the coaxial magnetic gear-based compact actuation module for small-to-mid-sized mechanical and robotic systems. Since the amplified torque by the gear ratio is remotely transmitted through magnetic coupling, the actuator provides backdrivability, hardware safety, and increased transparency compared to the traditional contact-based mechanical gear transmission. We also implemented a sensorless torque control algorithm using magnetic coupling property (i.e., magnetic spring) similar to that of the SEA. These features originate from the interesting mechanism of the coaxial magnetic gear combined with the transmission ratio amplifier (i.e., gearbox) and the magnetic spring in a single structure. Considering these features, the proposed actuation module lies between the quasi-direct drive and SEA, which has both characteristics.

While there are still several issues need to be addressed, we believe that the proposed non-contact transmission/actuation module may have many advantages in specific applications requiring overload projection, sealing, high-maintenance and remote power transfer. For instance, tool changers using the proposed actuator and controller would enable easy attachment/detachment of various tools with robust torque control. Also, robotic applications operating in harsh environments such as underwater, desert, and space can be applicable area.

IEEE Robotics and Automation Letters (RA-L) paper, presented at ICRA 2024, Yokohama, Japan. Cite as RA-L paper.

IEEE Robotics and Automation Letters (RA-L) paper, presented at ICRA 2024, Yokohama, Japan. Cite as RA-L paper.

The torque control bandwidth of the proposed actuation module is approximately 8Hz (see Fig. 11), which is relatively low in comparison to conventional contact-based actuators, but it can be attributed to its spring-like characteristic. This could be resolved by increasing the pole pair of the inner rotor at the design phase, which raises the stiffness in the aspect of mechanical angle.

The maximum transmittable torque was measured at 5.6 Nm, which follows the torque density of about 4.3Nm/kg. The maximum transmittable torque was 43% of the FEMM simulation result. We believe the discrepancy between reality and simulation stems from the end-effects [29]. In general, 2D FEMM overestimates the performance because it does not reflect the magnetic leakage and fringing represented by the end-effects [29]. To increase the toque density, applying Halbach array [30] to the inner and outer magnets is one of the solutions, which concentrates the magnetic field on one side.

VII. Conclusion

In this letter, we proposed a coaxial magnetic gear-based actuation module, its optimization and design procedure guideline, and a composite DOB-based torque control algorithm. The two mass spring dynamic model was derived and specified its characteristic. The DOB-based torque control algorithm was proposed utilizing the feature of the magnetic coupling (i.e., magnetic spring), which is the magnetic gear's spring-like characteristic. By directly manipulating the electrical deflection angle of the magnetic gear, we can facilitate the straightforward detection and compensation of pole-slip, thereby enabling robust torque control following pole-slip events. The prototype with a dimension of ϕ 90mm×15mm was made for the disc-type BLDC motor as a transmission ratio amplifier. Several experiments were conducted to validate the proposed design and controller. The controller showed a reasonable performance for the torque reference tracking without any extra torque/force sensor. Based on the torque controller, various impedance could be realized. The overload protection experiment demonstrated the robustness of the proposed controller under overload conditions without damaging the hardware and effective recovery capabilities following pole-slip occurrences.

References

[1] D. Hesmondhalgh and D. Tipping, "A multielement magnetic gear," in *IEE Proceedings B-Electric Power Applications*, vol. 127, no. 3. IET, 1980, pp. 129–138.

[2] K. Tsurumoto and S. Kikuchi, "A new magnetic gear using permanent magnet," *IEEE Transactions on Magnetics*, vol. 23, no. 5, pp. 3622–3624, 1987.

[3] K. Atallah and D. Howe, "A novel high-performance magnetic gear," *IEEE Transactions on magnetics*, vol. 37, no. 4, pp. 2844–2846, 2001.

[4] K. Atallah, S. Calverley, and D. Howe, "Design, analysis and realisation of a high-performance magnetic gear," *IEE Proceedings-Electric Power Applications*, vol. 151, no. 2, pp. 135–143, 2004.

[5] T. Lubin, S. Mezani, and A. Rezzoug, "Analytical computation of the magnetic field distribution in a magnetic gear," *IEEE Transactions on magnetics*, vol. 46, no. 7, pp. 2611–2621, 2010.

[6] M. Filippini and P. Alotto, "Coaxial magnetic gear design and optimization," *IEEE Transactions on Industrial Electronics*, vol. 64, no. 12, pp. 9934–9942, 2017.

[7] Y. Wang, M. Filippini, G. Bacco, and N. Bianchi, "Parametric design and optimization of magnetic gears with differential evolution method," *IEEE Transactions on Industry Applications*, vol. 55, no. 4, pp. 3445–3452, 2019.

[8] N. Niguchi and K. Hirata, "Cogging torque analysis of magnetic gear," *IEEE transactions on industrial electronics*, vol. 59, no. 5, pp. 2189–2197, 2011.

[9] E. Gouda, S. Mezani, L. Baghli, and A. Rezzoug, "Comparative study between mechanical and magnetic planetary gears," *IEEE transactions on magnetics*, vol. 47, no. 2, pp. 439–450, 2010.

[10] M. C. Gardner, B. Praslicka, M. Johnson, and H. A. Toliyat, "Optimization of coaxial magnetic gear design and magnet material grade at different temperatures and gear ratios," *IEEE Transactions on Energy Conversion*, vol. 36, no. 3, pp. 2493–2501, 2021.

[11] A. B. Kjaer, S. Korsgaard, S. S. Nielsen, L. Demsa, and P. O. Rasmussen, "Design, fabrication, test, and benchmark of a magnetically geared permanent magnet generator for wind power generation," *IEEE Transactions on Energy Conversion*, vol. 35, no. 1, pp. 24–32, 2019.

[12] H. Y. Wong, H. Baninajar, B. Dechant, and J. Bird, "Designing a magnetic gear for an electric aircraft drivetrain," in *2020 IEEE Energy Conversion Congress and Exposition (ECCE)*. IEEE, 2020, pp. 1–6.

[13] H. Shin, J. Chang, and D. Hong, "Design and characteristics analysis of coaxial magnetic gear for contra-rotating propeller in yacht," *IEEE Transactions on Industrial Electronics*, vol. 67, no. 9, pp. 7250–7259, 2019.

[14] Z. Ling, W. Zhao, P. O. Rasmussen, J. Ji, Y. Jiang, and Z. Liu, "Design and manufacture of a linear actuator based on magnetic screw transmission," *IEEE transactions on Industrial electronics*, vol. 68, no. 2, pp. 1095–1107, 2020.

[15] B. Praslicka, M. Johnson, E. Plugge, N. Palmer, D. F. Knight, A. White, T. Simms, D. Zamarron, and H. A. Toliyat, "Design and analysis of a novel, low-cost, high-speed cycloidal magnetic gear for aerospace servo actuator applications," *IEEE/ASME Transactions on Mechatronics*, 2023.

[16] E. Lee, H. Song, J. Jeong, and S. Jeong, "Mechanical variable magnetic gear transmission: Concept and preliminary research," *IEEE Robotics and Automation Letters*, vol. 7, no. 2, pp. 3357–3364, 2022.

[17] R. Montague, C. Bingham, and K. Atallah, "Servo control of magnetic gears," *IEEE/Asme Transactions on Mechatronics*, vol. 17, no. 2, pp. 269–278, 2011.

[18] ——, "Dual-observer-based position-servo control of a magnetic gear," *IET electric power applications*, vol. 5, no. 9, pp. 708–714, 2011.

[19] R. G. Montague, C. Bingham, and K. Atallah, "Magnetic gear pole-slip prevention using explicit model predictive control," *IEEE/ASME Transactions on Mechatronics*, vol. 18, no. 5, pp. 1535–1543, 2012.

[20] H. Komiyama and Y. Uchimura, "Speed control and sensorless force control with magnetic gear," in *2010 11th IEEE International Workshop on Advanced Motion Control (AMC)*. IEEE, 2010, pp. 325–330.

[21] ——, "Contactless magnetic gear for robot control application," *Electrical Engineering in Japan*, vol. 184, no. 4, pp. 32–41, 2013.

[22] H. Song, E. Lee, and S. Jeong, "Magnetic gear based actuator: Design and optimization," in *2022 22nd International Conference on Control, Automation and Systems (ICCAS)*. IEEE, 2022, pp. 1039–1043.

[23] S. Seok, A. Wang, D. Otten, and S. Kim, "Actuator design for high force proprioceptive control in fast legged locomotion," in *2012 IEEE/RSJ International Conference on Intelligent Robots and Systems*. IEEE, 2012, pp. 1970–1975.

[24] B. Praslicka, M. C. Gardner, M. Johnson, and H. A. Toliyat, "Review and analysis of coaxial magnetic gear pole pair count selection effects," *IEEE Journal of Emerging and Selected Topics in Power Electronics*, vol. 10, no. 2, pp. 1813–1822, 2021.

[25] D. C. Meeker, "Finite element method magnetics," https://www.femm.info, Version 4.2 (21Apr2019 Build), [Online; accessed 06-March-2023].

[26] J. R. Ryoo, T.-Y. Doh, and M. J. Chung, "Robust disturbance observer for the track-following control system of an optical disk drive," *Control Engineering Practice*, vol. 12, no. 5, pp. 577–585, 2004.

[27] N. Paine, S. Oh, and L. Sentis, "Design and control considerations for high-performance series elastic actuators," *IEEE/ASME Transactions on Mechatronics*, vol. 19, no. 3, pp. 1080–1091, 2013.

[28] S. Oh and K. Kong, "High-precision robust force control of a series elastic actuator," *IEEE/ASME Transactions on mechatronics*, vol. 22, no. 1, pp. 71–80, 2016.

[29] S. Gerber and R. Wang, "Analysis of the end-effects in magnetic gears and magnetically geared machines," in *2014 International Conference on Electrical Machines (ICEM)*. IEEE, 2014, pp. 396–402.

[30] L. Jian and K. Chau, "A coaxial magnetic gear with halbach permanent-magnet arrays," *IEEE Transactions on Energy conversion*, vol. 25, no. 2, pp. 319–328, 2010.

IEEE Robotics and Automation Letters (RA-L) paper, presented at ICRA 2024, Yokohama, Japan. Cite as RA-L paper.